Progress In Electromagnetics Research, Vol. 171, 137–158, 2021

Calculations of Bands and Band Field Solutions in Topological Acoustics Using the Broadband Green's Function-KKR-Multiple Scattering Method

Leung Tsang[1], Tien-Hao Liao[2, *], and Shurun Tan[3, 4, 5]

Abstract—In this paper, we apply the BBGF-KKR-MST (Broadband Green's function-KKR-Multiple Scattering Theory) to calculate Band Structures and Band Field Solutions in topological acoustics. A feature of BBGF is that the lattice Green's functions are broadband, and the transformations to cylindrical waves are calculated rapidly for many frequencies for speedy calculation of the determinant of the KKR equation. For the two bands of interest, only 5 cylindrical waves are sufficient so that the dimension of the eigenvalue matrix equation is only 5. The CPU time requirement, including setup and using MATLAB on a standard laptop, is 5 milliseconds for a band eigenvalue. Using the eigenvalue and scattered field eigenvector, the field in the cell is calculated by higher order cylindrical waves. The exciting field of higher order cylindrical waves requires only 11 coefficients to represent the band field solutions in the cell. Comparisons are made with the results of the volume integral equation method and the commercial software COMSOL. The BBGF-KKR-MST method is significantly faster.

1. INTRODUCTION

Topological states in photonics were initially proposed by Haldane in analogy to the quantum Hall (QH) effect in electronic systems. Topologically protected, unidirectional, backscattering-free edge states immune to distortions have been observed in topological photonics, using photonic crystals with gyrotropic constituents placed in an applied dc magnetic field [1]. Similar phenomena have also been reported in topological acoustics [2, 3].

The calculation of band diagrams and band field solutions for topological photonics and topological acoustics have been studied recently [4, 5]. The common method of band calculations is the plane wave method [6–9]. The advantage of the plane wave method is that the eigenvalue problem is a linear eigenvalue problem. The disadvantage of the method is the poor convergence of the plane waves requiring a large number of plane waves. For a 2D problem, it requires several thousand plane waves to achieve convergence particularly for sharp contrast between the scatterer and the background host materials. The plane wave method gives an eigenvalue problem of matrix dimension of several thousands. Discrete methods such as the finite difference method (FDM) [10, 11] and the finite element method (FEM) [12, 13] have also been used. The commercial software COMSOL which has been extensively used in simulations of photonic crystals and phononic crystals is based on FEM. The disadvantages of the FDM and FEM methods are that volumetric discretization of the unit cell is required. For a 2D

Received 17 August 2021, Accepted 17 October 2021, Scheduled 22 October 2021

* Corresponding author: Tien-Hao Liao (thliao@caltech.edu).

[1] Radiation Laboratory, Department of Electrical Engineering and Computer Science, University of Michigan, Ann Arbor, MI 48109, USA. [2] Division of Geological and Planetary Sciences, California Institute of Technology, Pasadena, CA 91125, USA. [3] Zhejiang University/University of Illinois at Urbana-Champaign Institute, Zhejiang University, Haining, Zhejiang 314400, China. [4] State Key Laboratory of Modern Optical Instrumentation, College of Information Science and Electronic Engineering, Zhejiang University, Hangzhou 310027, China. [5] Department of Electrical and Computer Engineering, University of Illinois at Urbana-Champaign, Urbana, IL 61801, USA.

problem, it requires such as ten thousand points or elements for volumetric discretization giving an eigenvalue problem of matrix dimension of around ten thousand.

The Korringa-Kohn-Rostoker method (KKR) [14–16] and multiple scattering theory (MST) [17–19] were also applied. The Multiple Scattering method initially proposed by Foldy [17] and Lax [18] has been used for decades in many areas. In remote sensing [20, 21] and in waveguides [22, 23], the method is labelled as Foldy-Lax (FL) multiple scattering equations. In optical scattering [24, 25], it is labelled as superposition T matrix method, after Waterman's pioneering work [26]. It has been applied in band structures calculations [27], quasicrystals [28], electron diffraction [29–31], and quantum many body theories in random lasers [32]. To improve computational efficiency, an FFT-based method known as "sparse matrix canonical grid method has also been proposed [33]. However, in its common form, even with numerical improvement, MST is not efficient for band diagram and band fields of periodic structures such as in photonic crystals. This is because the common MST method is a single frequency method. The solution is computed at a given frequency. The CPU of computing the solutions at many frequencies, such as at 100 frequencies, is 100 times that of the CPU of a single frequency. In band diagram problems of periodic structures, the frequency is unknown. One has to first determine the frequency which is the eigenvalue of the multiple scattering equation. To perform the calculations with the single frequency method MST, one has to solve the MST equations repeatedly for tens and hundreds of frequencies and then determine the frequency eigenvalues. Recently, researchers in the field of photonic crystals and phononic crystals have been using the Finite Element method (FEM) [12, 13] and the finite difference method (FDM) [11]. The advantage of FEM is that although the number of unknowns is large in FEM, the eigenvalue problem is linear in FEM so that the band field solutions for the first few bands are computed efficiently. In addition, the FEM method is applied to a single cell, and the Bloch conditions are imposed readily on opposite sides of the cell boundary [12, 13]. Simulations of band diagrams of topological photonic and topological phonon crystals are largely based on COMSOL [34–36]. KKR refers to eigenvalue equation from which the band eigenvalue frequency for a given Bloch vector is determined. KKR equation can be derived by various methods. In this paper, we use MST method to derive KKR equation. Based on the single scatterer T-matrix in MST, we show that the dimension of the KKR eigenvalue equation is small, and the dimension is only 5 by 5 in this paper.

Recently we developed Broadband Green's functions (BBGF) method [5, 37–41] for band diagram calculations that has two distinct features. Firstly, after an initial setup is completed, the calculations for many frequencies are performed rapidly, making the method broadband. Secondly, unlike classical expansions of Green's functions which are poorly convergent, the BBGF expansions are rapidly convergent by making use of imaginary wavenumber extractions [42, 43]. We have implemented BBGF in band calculations in two methods. In the first method, the solutions were obtained by combining the BBGF with the integral equation and solved by the method of moment (MoM). The method is labelled as the BBGF-MoM method [5, 37–39]. Recently we proposed the second method [40, 41] in which we combined the Broadband Green's function (BBGF) method with the KKR method and the Multiple Scattering Theory (MST). We label the method as BBGF-KKR-MST. In the usual KKR method, the lattice Green's function which is the periodic Green's function without the plurality of scatterers is calculated. The convergence of the lattice Green's function is accelerated by the Ewald method which is a single frequency method. In BBGF, we use the Broadband Green's function to derive analytic expressions of the broadband transformation to cylindrical waves. The method requires a setup after which the determinant for many frequencies is computed readily. Thus, for broadband calculations, the BBGF method is much faster than the Ewald method [42, 43]. In the formulation, we utilize the MST in which the band eigenvalue problem is expressed in terms of the single scatterer T matrix of the scatterer. The size of the matrix can be made small because in deriving the matrix equation, the exciting fields are in the extinction region of the scatterer so that low order cylindrical waves can be used. After the eigenvalues are solved, the field throughout the entire cell is calculated by higher order cylindrical waves. We have applied the BBGF-KKR-MSR method to topological photonics, and it is shown that the BBGF-KKR-MST method is significantly faster than COMSOL [40, 41].

In previous work of topological bands, we have applied the BBGF-KKR-MST method to topological photonics [40, 41]. In this paper, we apply the method to topological acoustics. In applying the MST, which is the same as the Foldy-Lax multiple scattering equations [44–48], we utilize the concept of "the

final exciting field" and "the final scattered field". For the eigenvalue equation, the final exciting field is inside the scatterer region by the extinction theorem. We demonstrate the topological acoustics for the case of scatterer of radius $b = 0.4a$, where a is the lattice constant. A low order of 2nd order cylindrical waves is sufficient for the 2 bands of interests, and the eigenvalue equation is only of dimension 5 by 5 based on the cylindrical wave harmonics of $n = 0, \pm 1, \pm 2$. After obtaining the eigenvector of surface fields, the higher order cylindrical waves are used to compute the fields for the (0,0) cell. The higher order cylindrical waves include higher harmonics for the band fields inside the entire (0,0) cell. For the example illustrated, these are carried $n = 0, \pm 1, \ldots, \pm 5$. It means that the band fields in the cell are represented by merely 11 cylindrical wave coefficients. This count is much less than volumetric methods of discretization of FEM and FDM where the number of field values is the same as the number of discretized points in the cell.

The outline of the paper is as follows. In Section 2, we derive the integral equations of the BBGF-KKR-MST method. In Section 3, the cylindrical wave expansions are used in solving the integral equations. In Section 4, the eigen-value matrix equation is derived using the single scatterer T matrix. In Section 5, the calculation of fields is described using higher order cylindrical waves. In Section 6, we calculate the T matrix for the problem of rotating fluid of Reference [2]. The normalization of the band fields is done analytically in Section 7. Numerical results and CPU requirements are described in Section 8.

2. MST FORMULATION OF INTEGRAL EQUATIONS IN PERIODIC STRUCTURES

The multiple scattering theory (MST) formulation is used to derive the integral equations for general scatterers. Consider a periodic lattice with lattice constant a. Let the cells be labeled as (m, n). Consider the $(0, 0)$ cell (Figure 1). The scatterer is of arbitrary shape and is enclosed by a circular boundary S_B of radius b. Let S_C be the boundary of the $(0, 0)$ cell. We use V_1 to denote the region inside S_B (including the arbitrarily shaped scatterer) and V_0 the region outside the scatterer region V_1 and is within the cell $(0, 0)$. Let ψ be the wave function in V_0 that satisfies the wave equation

$$\left(\nabla^2 + k^2\right) \psi = 0 \tag{1}$$

where $k = \omega/c$ is the wavenumber of the background medium, ω the angular frequency, and c the acoustic wave velocity in the background medium. Setting c equal to unity, the normalized frequency is $f_N = k/(2\pi)$. We only need to solve the band fields in $(0, 0)$ cell as fields in other cells can be obtained by applying Bloch theorem.

In MST, the formulation is performed for a single isolated scatterer. The wave function ψ is the sum of ψ^{ex}, the "final" exciting field, and ψ^s the "final" scattered field. Both ψ^{ex} and ψ^s refers to that of the "single scatterer" that resides inside V_1. The self-consistent equations of MST allow ψ^{ex} and ψ^s to be calculated in a self-consistent manner [44, 45].

$$\psi\left(\bar{r}\right) = \psi^{ex}\left(\bar{r}\right) + \psi^s\left(\bar{r}\right); \quad \text{for } \bar{r} \quad \text{in } V_0 \tag{2}$$

Using extinction theorem, $\psi^{ex}(\bar{r})$ is also defined in V_1. Thus, ψ^{ex} exists in V_0 and in V_1. The exciting field obeys the equation with the wave number k even though $\bar{r}$ can be in V_1.

$$\left(\nabla^2 + k^2\right) \psi^{ex} = 0; \quad \text{for } \bar{r} \text{ in } V_0 \text{ and in } V_1 \tag{3}$$

Because ψ^s is the scattered field from the single scatterer, it exists outside the scatterer. It exists in V_0 and outside the cell all the way to infinity.

$$\left(\nabla^2 + k^2\right) \psi^s = 0; \quad \text{for } \bar{r} \text{ in } V_0 \text{ and to infinity} \tag{4}$$

For a Bloch vector $\bar{k}_i$ let $g_P(k, \bar{k}_i, \bar{r}, \bar{r}')$ be the lattice Green's function. The lattice Green's function is a function of k and $\bar{k}_i$. The lattice Green's function g_P obeys the Bloch theorem and obeys the wave equation

$$\left(\nabla^2 + k^2\right) g_P\left(k, \bar{k}_i, \bar{r}, \bar{r}'\right) = -\delta\left(\bar{r} - \bar{r}'\right); \quad \text{where } \bar{r} \text{ and } \bar{r}' \text{ can be in } V_0 \text{ or } V_1 \tag{5}$$

The $g_P(k, \bar{k}_i, \bar{r}, \bar{r}')$ is the periodic Green's function for an empty lattice. Thus, the $\bar{r}$ and $\bar{r}'$ can be in V_0 or V_1.

Using Green's theorem, it can be shown that the following equation holds

$$\int_{S_B} dl' \left[\psi\left(\bar{r}'\right)\hat{n}'\cdot\nabla' g_P\left(k,\bar{k}_i,\bar{r},\bar{r}'\right) - g_P\left(k,\bar{k}_i,\bar{r},\bar{r}'\right)\hat{n}'\cdot\nabla'\psi\left(\bar{r}'\right)\right] = \begin{cases} 0 & \text{for } \bar{r} \text{ in } V_1 \\ \psi\left(\bar{r}\right) & \text{for } \bar{r} \text{ in } V_0 \end{cases} \tag{6}$$

where $\int_{S_B} dl'$ is integration over S_B.

In the $(0,0)$ cell, the lattice Green's function $g_P(k,\bar{k}_i,\bar{r},\bar{r}')$ can be written as a sum of the free space Green's function $g_0(k,\bar{r},\bar{r}')$ and the response Green's function $g_R(k,\bar{k}_i,\bar{r},\bar{r}')$.

$$g_P\left(k,\bar{k}_i,\bar{r},\bar{r}'\right) = g_0\left(k,\bar{r},\bar{r}'\right) + g_R\left(k,\bar{k}_i,\bar{r},\bar{r}'\right) \tag{7}$$

where the free space Green's function is $g_0(k,\bar{r},\bar{r}') = \frac{i}{4}H_0^{(1)}(k\,|\bar{r}-\bar{r}'|)$, and it obeys the wave equation

$$\left(\nabla^2 + k^2\right) g_0\left(k,\bar{r},\bar{r}'\right) = -\delta\left(\bar{r}-\bar{r}'\right) \tag{8}$$

The response Green's function obeys the homogeneous wave equation

$$\left(\nabla^2 + k^2\right) g_R\left(k,\bar{k}_i,\bar{r},\bar{r}'\right) = 0 \tag{9}$$

The physical interpretation of $g_P(k,\bar{k}_i,\bar{r},\bar{r}')$ is the scattering from all cells while $g_R(k,\bar{k}_i,\bar{r},\bar{r}')$ is the scattering from other cells into the $(0,0)$ cell. Integral equations are next derived based on whether $\bar{r}$ is in V_0 or V_1.

2.1. Integral Equations with $\bar{r}$ in V_1

Since both ψ^{ex} and g_P can be in V_1 we apply Green's theorem by volumetric integration $d\bar{r}'$ over V_1 with $\bar{r}$ in V_1

$$\begin{aligned} &\iint_{V_1} d\bar{r}' \left[\psi^{ex}\left(\bar{r}'\right)\nabla'^2 g_P - g_P\nabla'^2\psi^{ex}\left(\bar{r}'\right)\right] \\ &= \int_{S_B} dl' \left[\psi^{ex}\left(\bar{r}'\right)\hat{n}'\cdot\nabla' g_P\left(k,\bar{k}_i,\bar{r},\bar{r}'\right) - g_P\left(k,\bar{k}_i,\bar{r},\bar{r}'\right)\hat{n}'\cdot\nabla'\psi^{ex}\left(\bar{r}'\right)\right] \\ &= -\psi^{ex}\left(\bar{r}\right) \text{ for } \bar{r} \text{ in } V_1 \end{aligned} \tag{10}$$

Subtracting Equation (10) from Equation (6) and using Equation (2) gives

$$\psi^{ex}\left(\bar{r}\right) = \int_{S_B} dl' \left[\psi^{s}\left(\bar{r}'\right)\hat{n}'\cdot\nabla' g_P\left(k,\bar{k}_i,\bar{r},\bar{r}'\right) - g_P\left(k,\bar{k}_i,\bar{r},\bar{r}'\right)\hat{n}'\cdot\nabla'\psi^{s}\left(\bar{r}'\right)\right] \tag{11}$$

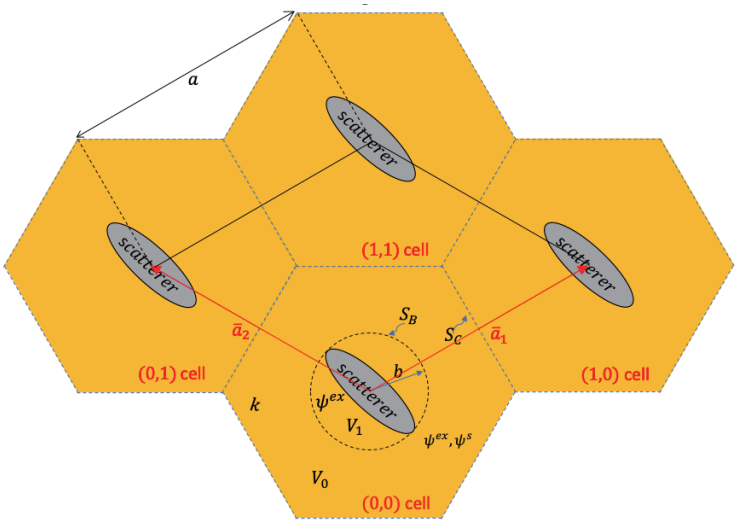

Figure 1. Periodic hexagonal cells with identical scatterers. In the $(0,0)$ cell: scatterer enclosed by circle of radius b; V_1: scatterer region; V_0: outside circle of radius b and within the $(0,0)$ cell; ψ^s: scattered field in V_0; ψ^{ex}: exciting field in both V_0 and V_1; $\bar{a}_1$ and $\bar{a}_2$ are primitive lattice vectors.

Next integration of $d\bar{r}'$ over V_0 and to infinity, and applying radiation boundary condition

$$\begin{aligned}&\iint_{V_0 \text{ and to infinity}} d\bar{r}' \left[\psi^s\left(\bar{r}'\right)\nabla'^2 g_0 - g_0 \nabla'^2 \psi^s\left(\bar{r}'\right)\right] = 0\\ &= \int_{S_B} dl' \left[\psi^s\left(\bar{r}'\right)\hat{n}'\cdot\nabla' g_0 - g_0 \hat{n}'\cdot\nabla'\psi^s\left(\bar{r}'\right)\right] \end{aligned} \tag{12}$$

Subtraction of (12) from (11) gives

$$\psi^{ex}\left(\bar{r}\right) = \int_{S_B} dl' \left[\psi^s\left(\bar{r}'\right)\hat{n}'\cdot\nabla' g_R\left(k,\bar{k}_i,\bar{r},\bar{r}'\right) - g_R\left(k,\bar{k}_i,\bar{r},\bar{r}'\right)\hat{n}'\cdot\nabla'\psi^s\left(\bar{r}'\right)\right] \tag{13}$$

The physical interpretation of Equation (13) is the scattering from other cells into cell $(0,0)$ resulting in the exciting field.

2.2. Integral Equations with $\bar{r}$ in V_0

We carry out volumetric integration $d\bar{r}'$ in $V_0 + V_1$ with $\bar{r}$ in $V_0 + V_1$

$$\begin{aligned}&\iint_{V_1+V_0} d\bar{r}' \left[\psi^{ex}\left(\bar{r}'\right)\nabla'^2 g_P - g_P \nabla'^2 \psi^{ex}\left(\bar{r}'\right)\right]\\ &= \int_{S_C} dl' \left[\psi^{ex}\left(\bar{r}'\right)\hat{n}'\cdot\nabla' g_P\left(k,\bar{k}_i,\bar{r},\bar{r}'\right) - g_P\left(k,\bar{k}_i,\bar{r},\bar{r}'\right)\hat{n}'\cdot\nabla'\psi^{ex}\left(\bar{r}'\right)\right]\\ &= -\psi^{ex}\left(\bar{r}\right) \quad \bar{r} \text{ in } V_0 + V_1 \end{aligned} \tag{14}$$

where $\int_{S_C} dl'$ is integration over the cell boundary S_C (Figure 1). Next, we carry out volumetric integral $d\bar{r}'$ in V_0. Then

$$\begin{aligned}&\iint_{V_0} d\bar{r}' \left[\psi^{ex}\left(\bar{r}'\right)\nabla'^2 g_P\left(k,\bar{k}_i,\bar{r},\bar{r}'\right) - g_P\left(k,\bar{k}_i,\bar{r},\bar{r}'\right)\nabla'^2\psi^{ex}\left(\bar{r}'\right)\right]\\ &= \int_{S_C} dl' \left[\psi^{ex}\left(\bar{r}'\right)\hat{n}'\cdot\nabla' g_P\left(k,\bar{k}_i,\bar{r},\bar{r}'\right) - g_P\left(k,\bar{k}_i,\bar{r},\bar{r}'\right)\hat{n}'\cdot\nabla'\psi^{ex}\left(\bar{r}'\right)\right]\\ &\quad - \int_{S_B} dl' \left[\psi^{ex}\left(\bar{r}'\right)\hat{n}'\cdot\nabla' g_P\left(k,\bar{k}_i,\bar{r},\bar{r}'\right) - g_P\left(k,\bar{k}_i,\bar{r},\bar{r}'\right)\hat{n}'\cdot\nabla'\psi^{ex}\left(\bar{r}'\right)\right] = -\psi^{ex}\left(\bar{r}\right) \end{aligned} \tag{15}$$

Taking the difference (14) and (15) gives

$$\int_{S_B} dl' \left[\psi^{ex}\left(\bar{r}'\right)\hat{n}'\cdot\nabla' g_P\left(k,\bar{k}_i,\bar{r},\bar{r}'\right) - g_P\left(k,\bar{k}_i,\bar{r},\bar{r}'\right)\hat{n}'\cdot\nabla'\psi^{ex}\left(\bar{r}'\right)\right] = 0 \quad \bar{r} \text{ in } V_0 \tag{16}$$

Take the difference of (16) and (6), and using (2), then gives

$$\psi\left(\bar{r}\right) = \int_{S_B} dl' \left[\psi^s\left(\bar{r}'\right)\hat{n}'\cdot\nabla' g_P\left(k,\bar{k}_i,\bar{r},\bar{r}'\right) - g_P\left(k,\bar{k}_i,\bar{r},\bar{r}'\right)\hat{n}'\cdot\nabla'\psi^s\left(\bar{r}'\right)\right] \quad \bar{r} \text{ in } V_0 \tag{17}$$

Next integrate $d\bar{r}'$ in V_0 and to infinity, and using radiation boundary condition

$$\begin{aligned}&\iint_{V_0 \,and\, to\, infinity} d\bar{r}' \left[\psi^s\left(\bar{r}'\right)\nabla'^2 g_0 - g_0\nabla'^2\psi^s\left(\bar{r}'\right)\right] = -\psi^s\left(\bar{r}\right)\\ &= -\int_{S_B} dl' \left[\psi^s\left(\bar{r}'\right)\hat{n}'\cdot\nabla' g_0 - g_0\,\hat{n}'\cdot\nabla'\psi^s\left(\bar{r}'\right)\right] \end{aligned} \tag{18}$$

Adding Eqs. (17) and (18), and using Equation (7) gives

$$\psi\left(\bar{r}\right) = \psi^s\left(\bar{r}\right) + \int_{S_B} dl' \left[\psi^s\left(\bar{r}'\right)\hat{n}'\cdot\nabla' g_R\left(k,\bar{k}_i,\bar{r},\bar{r}'\right) - g_R\left(k,\bar{k}_i,\bar{r},\bar{r}'\right)\hat{n}'\cdot\nabla'\psi^s\left(\bar{r}'\right)\right] \tag{19}$$

Using Eq. (2) in Eq. (19) means that $\bar{r}$ in V_0

$$\psi^{ex}\left(\bar{r}\right) = \int_{S_B} dl' \left[\psi^s\left(\bar{r}'\right)\hat{n}'\cdot\nabla' g_R\left(k,\bar{k}_i,\bar{r},\bar{r}'\right) - g_R\left(k,\bar{k}_i,\bar{r},\bar{r}'\right)\hat{n}'\cdot\nabla'\psi^s\left(\bar{r}'\right)\right] \tag{20}$$

Equation (20) looks the same as Equation (13). The difference is that Equation (13) has $\bar{r}$ in V_1 while Equation (20) has $\bar{r}$ in V_0. Thus, the number of terms in the cylindrical wave expansion of $\psi^{ex}(\bar{r})$ will be different between Eqs. (13) and (20). The physical interpretation of Eqs. (13) and (20) is that $\psi^{ex}(\bar{r})$ is the scattering from scatterers in other cells into the cell $(0,0)$. For physical interpretation $\int_{S_B} dl' \left[\psi^s(\bar{r}')\,\hat{n}'\cdot\nabla' g_R\left(k,\bar{k}_i,x,y,x',y'\right) - g_R\left(k,\bar{k}_i,x,y,x',y'\right)\hat{n}'\cdot\nabla'\psi^s(\bar{r}')\right] = \psi^{so}$ where "so" denotes scattering from other cells into the cell $(0,0)$.

3. CYLINDRICAL WAVE EXPANSIONS

The final scattered field is in V_0 and all the way to infinity, which can be expressed as outgoing cylindrical waves. Using cylindrical coordinates (r,θ)

$$\psi^s(\bar{r}) = \sum_{n=-N_L}^{N_L} a_n^s H_n^{(1)}(kr)\, e^{in\theta} \tag{21}$$

where $H_n^{(1)}$ is the Hankel function of first kind.

The summation of the expansion is to $|n| = N_L$. In MST, the key expansion is the convergence of the final scattered field. We note that in photonic crystal, the band eigen-frequencies are usually in the range of $0 \le f_N \le 1.5$. The size of the scatterer is of small or moderate size compared with wavelength. Thus, the maximum cylindrical wave index N_L is not large. The exciting field, as given in Equations (13) and (20) are in two regions V_1 and V_0. The number of terms in the expansions in the two regions will be different. For $\bar{r}$ in V_1

$$\psi^{ex}(\bar{r}) = \sum_{n=-N_L}^{N_L} a_n J_n(kr)\, e^{in\theta} \quad \text{for } \bar{r} \text{ in } V_1 \tag{22}$$

The exciting field expansion, because of the Bessel function $J_n(kr)$, is a nonuniform convergent series. Due to $\bar{r}$ in V_1 in Eq. (22) we need only to match to the scattered field with the maximum index of N_L.

For $\bar{r}$ in V_0, r is much larger when it is close to the cell boundary so that the argument of the Bessel function can be much larger. We need to have more terms with a larger upper index of N_{cyl} in the expansion. Thus, we have

$$\psi^{ex}(\bar{r}) = \sum_{n=-N_{cyl}}^{N_{cyl}} a_n^C J_n(kr)\, e^{in\theta} \quad \text{for } \bar{r} \text{ in } V_0 \tag{23}$$

where $N_{cyl} \ge N_L$. We use two different symbols for the coefficients a_n and a_n^C to distinguish the two regions. The response Green's function, $g_R\left(k,\bar{k}_i,\bar{r},\bar{r}'\right)$, obeys the homogeneous wave equation. The expansion is expressed as

$$g_R\left(k,\bar{k}_i,\bar{r},\bar{r}'\right) = \sum_l \frac{i}{4}\tilde{D}_l\left(k,\bar{k}_i\right) J_l\left(k\left|\bar{r}-\bar{r}'\right|\right) e^{il\theta_{\bar{r}\bar{r}'}} \tag{24}$$

where J_l is the Bessel function of order l, and $\theta_{\bar{r}\bar{r}'}$ is the angle that the vector $\bar{r}-\bar{r}'$ makes with the x-axis. The merit of BBGF is that the lattice Green's function can be computed fast for multi-frequencies. The method consists of imaginary extractions and a setup of the frequency independent part. The lattice Green's functions are transformed into cylindrical waves, and broadband expressions of $\tilde{D}_l(k,\bar{k}_i)$ are obtained. This procedure enables $\tilde{D}_l(k,\bar{k}_i)$ to be computed fast for many frequencies which are useful for searching the eigenvalue frequency. The details and computations are described in the previous paper [40]. We will discuss the number of terms in $\sum_l$. The requirement is not for the convergence of $g_R(k,\bar{k}_i,\bar{r},\bar{r}')$, but the number of terms in Eq. (23) is to get correct results for the scattered field and the two exciting fields. Using translational addition theorem [44] in Eq. (24).

$$g_R\left(k,\bar{k}_i,\bar{r},\bar{r}'\right) = \frac{i}{4}\sum_l \tilde{D}_l\left(k,\bar{k}_i\right)\sum_n J_n(kr)\, e^{in\theta} J_{n-l}\left(kr'\right) e^{-i(n-l)\theta'} \tag{25}$$

Substituting into Equations (13) and (20), $\int_S dl' = b\int_0^{2\pi} d\theta'$ and performing the integration, we have

$$\int_S dl'\psi^S\left(\bar{r}'\right)\hat{n}'\cdot\nabla' g_R\left(k,\bar{k}_i,\bar{r},\bar{r}'\right) = \frac{i\pi bk}{2}\sum_n J_n\left(kr\right)e^{in\theta}\sum_{m=-N_L}^{N_L}\left[a_m^s H_m^{(1)}\left(kb\right)J_m'(kb)\right]\tilde{D}_{n-m}(k,\bar{k}_i) \quad (26)$$

and

$$-\int_S dl' g_R\left(k,\bar{k}_i,\bar{r},\bar{r}'\right)\hat{n}'\cdot\nabla'\psi^s\left(\bar{r}'\right) = -\frac{i\pi bk}{2}\sum_n J_n\left(kr\right)e^{in\theta}\sum_{m=-N_L}^{N_L}\left[a_m^s H_m^{(1)'}\left(kb\right)\right]\tilde{D}_{n-m}(k,\bar{k}_i)J_m(kb) \quad (27)$$

Combining and making use of the Wronskin [49] $H_m^{(1)'}\left(kb\right)J_m\left(kb\right) - H_m^{(1)}\left(kb\right)J_m'\left(kb\right) = i2/(\pi kb)$ we have

$$\begin{aligned}\psi^{ex}\left(\bar{r}\right) &= \int_{S_B} dl'\left[\psi^s\left(\bar{r}'\right)\hat{n}'\cdot\nabla' g_R\left(k,\bar{k}_i,\bar{r},\bar{r}'\right) - g_R\left(k,\bar{k}_i,\bar{r},\bar{r}'\right)\hat{n}'\cdot\nabla'\psi^s\left(\bar{r}'\right)\right]\\ &= \sum_n J_n\left(kr\right)e^{in\theta}\sum_{m=-N_L}^{N_L} a_m^s\tilde{D}_{n-m}\left(k,\bar{k}_i\right)\end{aligned} \quad (28)$$

From Eqs. (13) and (20), we have the same equation with different numbers of terms in the expansion of $\psi^{ex}(\bar{r})$.

4. EIGENVALUE PROBLEM AND SINGLE SCATTER *T* MATRIX IMPLEMENTATION

Comparing Equations (22) and (28)

$$\sum_{m=-N_L}^{N_L}\tilde{D}_{n-m}\left(k,\bar{k}_i\right)a_m^s = a_n; \quad n = 0,\pm1,\ldots,\pm N_L \quad (29)$$

which is the eigenvalue equation.

The dimension of the eigenvalue equation is $2N_L+1$. Because the index of $\tilde{D}_{n-m}$ is $n-m$ we need to compute $\tilde{D}_l(k)$, $l = 0,\pm1,\ldots,\pm N_{DL}$ with

$$N_{DL} = 2N_L \quad (30)$$

The eigenvalue Equation (29) can be put in matrix form of dimension $2N_L+1$, by using indices in the following order: $-N_L, -N_L+1,\ldots,-1,0,1,\ldots,N_L-1,N_L$. In matrix form

$$\bar{a} = \overline{\overline{\tilde{D}}}\bar{a}^s \quad (31)$$

where

$$\left[\overline{\overline{\tilde{D}}}\right]_{nm} = \tilde{D}_{n-m}; \quad n,m = -N_L,\ldots,-1,0,1,\ldots,N_L \quad (32)$$

As discussed in Section 2, the MST formulation uses the concept of isolated single scatterer. The relation between scattered field and exciting field is through the single scatterer T matrix coefficients $T_{mn}(k)$. The T matrix $T_{mn}(k)$ is independent of the Bloch vector $\bar{k}_i$. The scattered field and T-matrix coefficients exist outside the circle with radius b.

$$a_m^s = \sum_{n=-N_L}^{N_L} T_{mn}\left(k\right)a_n; \quad m = -N_L,\ldots,0,\ldots,N_L \quad (33)$$

Using the matrix notations

$$\bar{a}^s = \overline{\overline{T}}\bar{a} \quad (34)$$

where $\bar{a}^s$ and $\bar{a}^s$ are column vectors of dimension $2N_L+1$, containing respectively the scattered field and exciting field coefficients respectively. Substituting Eq. (34) in Eq. (31). we have the matrix eigenvalue equation

$$\overline{\overline{S}}\,(k)\,\bar{a}=0 \tag{35}$$

where

$$\overline{\overline{S}}=\overline{\overline{I}}-\overline{\overline{\tilde{D}}}\,\overline{\overline{T}} \tag{36}$$

where $\overline{\overline{I}}$ is the unit matrix of dimension $2N_L+1$. The eigenvector is the exciting field coefficients $\bar{a}$. Next, we convert the eigenvalue equation into one with eigenvector being the scattered field coefficients $\bar{a}^s$. Let $\bar{\bar{t}}$ be related to the inverse of the T matrix as follows

$$\overline{\overline{T}}^{-1}=-\overline{\overline{I}}-i\bar{\bar{t}} \tag{37}$$

Then we obtain

$$\overline{\overline{\Lambda}}\,(k)\,\bar{a}^s=0 \tag{38}$$

where

$$\overline{\overline{\Lambda}}=\overline{\overline{D}}-\frac{1}{4}\bar{\bar{t}} \tag{39}$$

and

$$\overline{\overline{D}}=\frac{i}{4}\left(\overline{\overline{\tilde{D}}}+\overline{\overline{I}}\right) \tag{40}$$

Equations (38) and (39) are labelled as "KKR determinant equation". In index notations

$$D_{nm}=D_{n-m}=\frac{i}{4}\left(\tilde{D}_{n-m}+\delta_{nm}\right) \tag{41}$$

$$\Lambda_{nm}=D_{n-m}-\frac{1}{4}t_{nm} \tag{42}$$

where δ_{nm} is the Kronecker delta. The T matrix is that of an isolated single scatterer and is independent of the lattice and independent of the Bloch vector $\bar{k}_i$. Furthermore, the T matrix is a smooth function of k because the scatterer size is small to moderate in the frequency range of interest.

After Equation (38) is solved, the eigenvalue k is determined. The normalized frequency $f_N = k/(2\pi)$ of the band at the Bloch vector $\bar{k}_i$ is determined. The eigenvector $\bar{a}^s$ and $\bar{a}$ are determined.

5. HIGHER ORDER CYLINDRICAL WAVES IN REGION V_0

After the eigenvalue k, the eigenvector $\bar{a}^s$ and $\bar{a}$ are determined, and we need to calculate the field in V_0 using Equations (21) and (23).

$$\psi\left(\bar{r}\right)=\psi^s\left(\bar{r}\right)+\psi^{ex}\left(\bar{r}\right)=\sum_{n=-N_L}^{N_L}a_n^sH_n^{(1)}\left(kr\right)e^{in\theta}+\sum_{n=-N_{cyl}}^{N_{cyl}}a_n^CJ_n\left(kr\right)e^{in\theta} \tag{43}$$

Comparing Equations (23) and (28)

$$a_n^C=\sum_{m=-N_L}^{N_L}a_m^s\tilde{D}_{n-m}(k);\quad n=0,\pm1,\ldots,\pm N_L,\ldots,\pm N_{cyl} \tag{44}$$

The index of a_n^C is higher at N_{cyl}. Because the locations in V_0 have larger r than that of the locations in V_1, we need to go to higher order cylindrical waves $N_{cyl}\geq N_L$.

For the scattered field $\bar{a}_m^s, m=0,\pm1,\ldots,\pm N_L$. Because the index of $\tilde{D}_{n-m}$ is $n-m$, we need to compute $\tilde{D}_l\left(k\right)$, $l=0,\pm1,\ldots,\pm N_L,\ldots,\pm(N_L+N_{cyl})$, with the determined k. Comparing Eqs. (29) and (44), we have

$$a_n^C=\begin{cases}a_n & \text{for}=0,\pm1,\ldots,\pm N_L\\ \displaystyle\sum_{m=-N_L}^{N_L}a_m^s\tilde{D}_{n-m}\left(k,\bar{k}_i\right) & \text{for } n=\pm\left(N_L+1\right),\ldots,\pm N_{cyl}\end{cases} \tag{45}$$

The second half of Equation (45) gives the equation to compute the higher order coefficients a_n^C of the exciting field $\psi^{ex}(\bar{r})$.

6. *T* MATRIX FOR THE ACOUSTIC SCATTERER OF ROTATING FLUID

The equations developed in previous sections are applicable to scatterers with an arbitrary shape characterized by an isolated single scatterer T matrix $T_{mn}(k)$. In this Section we derive the T matrix for the circular acoustic scatterer of rotating fluid which is used in [2]. The fluid field equations are complicated in the rotating region. We started with the acoustic master equation of the velocity potential, but used a simplified version that neglects the secondary effects from the spatial gradient of the ambient sound speed c, air density, high order terms of $v_0 \ll c$, and the quadratic terms of $\bar{A}$. We thus have Equation (2) of reference [39] which will be solved in this paper. The rotating fluids are in the region $r_1 \leq r \leq r_2$ (Figure 2).

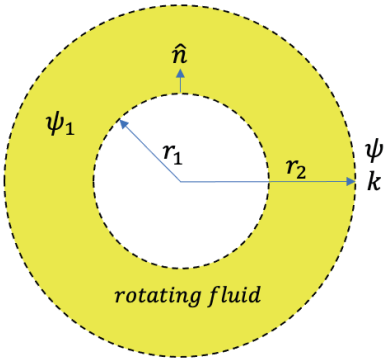

Figure 2. Circular scatterer of rotating fluid, rotating in $r_1 \leq r \leq r_2$; Neumann boundary condition $\partial\psi_1/\partial n = 0$ at $r = r_1$.

For this case, $b = r_2$, the wave function in $r_1 \leq r \leq r_2$ is ψ_1. The simplified linearized wave equation with the above approximations is in [42]

$$\left(\nabla^2 + k^2\right)\psi_1 = i2\bar{A} \cdot \nabla\psi_1 \tag{46}$$

where $\bar{A} = \frac{\omega \bar{v}_0(\bar{r})}{c^2}$ and the angular velocity, $\bar{v}_0(\bar{r})$, of the rotating fluid is

$$\bar{v}_0(\bar{r}) = \hat{\theta}\frac{\Omega r_1^2}{r_2^2 - r_1^2}\left(-r + \frac{r_2^2}{r}\right) \tag{47}$$

In Equation (47), Ω is the angular velocity of radians/sec at r_1. Note that the angular velocity, $\bar{v}_0(\bar{r})$, is 0 at r_2. The boundary conditions are that $\partial\psi_1/\partial r = 0$ at $r = r_1$. The wave functions and normal derivatives are continuous at $r = r_2$.

Because the scatterer is circular, the T matrix is diagonal with $T_{mn}(k) = \delta_{mn}T_n(k)$. Then the wave equation is

$$\frac{\partial^2\psi_1}{\partial r^2} + \frac{1}{r}\frac{\partial\psi_1}{\partial r} + \frac{1}{r^2}\frac{\partial^2\psi_1}{\partial\theta^2} + k^2\psi_1 = -i2\frac{\omega}{c^2}\frac{\Omega r_1^2}{r_2^2 - r_1^2}\left(-r + \frac{r_2^2}{r}\right)\frac{1}{r}\frac{\partial\psi_1}{\partial\theta} for r_1 < r < r_2 \tag{48}$$

To solve Equation (48), let

$$\psi_1 = \sum_{n=-N_L}^{N_L} c_n(r)e^{in\theta} \tag{49}$$

where n are integers. We truncate the summation at the same order $\pm N_L$ as that of the scattered wave. Substituting in Eq? (48) and simplifying, we obtain the second order differential equation for $c_n(r)$

$$\frac{d^2c_n(r)}{dr^2} + \frac{1}{r}\frac{dc_n(r)}{dr} + c_n(r)\,k_1^2 - \frac{c_n(r)}{r^2}\nu^2 = 0 \tag{50}$$

where

$$k_1^2 = k^2 + 2n\frac{\omega}{c^2}\frac{\Omega r_1^2}{r_2^2 - r_1^2} \tag{51}$$

$$\nu^2 = n^2 + r_2^2 2n\frac{\omega}{c^2}\frac{\Omega r_1^2}{r_2^2 - r_1^2} \tag{52}$$

The solutions of Eq. (50) are Bessel functions of non-integer order ν. We write in terms of $J_\nu(k_1 r)$ and $N_\nu(k_1 r)$ which are Bessel function and Neumann function of non-integer order ν. Let

$$\psi_1(\bar{r}) = \sum_{n=-N_L}^{N_L} \left[c_n J_\nu(k_1 r) + d_n N_\nu(k_1 r)\right] e^{in\theta} \tag{53}$$

The boundary conditions are Neumann boundary condition $\partial\psi_1/\partial r = 0$ at $r = r_1$ and continuity of fields and normal derivatives at $r = r_2$.

$$\frac{\partial \psi_1}{\partial r}(r = r_1) = 0 \tag{54}$$

$$\psi_1(r = r_2) = \psi(r = r_2) = \sum_{n=-N_L}^{N_L} \left[a_n J_n(kr_2) + a_n^s H_n^{(1)}(kr_2)\right] e^{in\theta} \tag{55}$$

$$\left.\frac{\partial \psi_1}{\partial r}\right|_{r=r_2} = \left.\frac{\partial \psi}{\partial r}\right|_{r=r_2} = k \sum_{n=-N_L}^{N_L} \left[a_n J_n'(kr_2) + a_n^s H_n^{(1)'}(kr_2)\right] e^{in\theta} \tag{56}$$

These give three simultaneous linear equations relating the coefficients a_n, a_n^s, c_n, and d_n. Solving the simultaneous equations give

$$d_n = p_n c_n \tag{57}$$

where

$$p_n = -\frac{J_\nu'(k_1 r_1)}{N_\nu'(k_1 r_1)} \tag{58}$$

Since,

$$a_n^s = T_n a_n \tag{59}$$

We obtain

$$T_n = -\frac{k_1 q_n J_n(kr_2) - kJ_n'(kr_2)}{k_1 q_n H_n^{(1)}(kr_2) - kH_n^{(1)'}(kr_2)} \tag{60}$$

$$q_n = \frac{J_\nu'(k_1 r_2) + p_n N_\nu'(k_1 r_2)}{J_\nu'(k_1 r_2) + p_n N_\nu'(k_1 r_2)} \tag{61}$$

We also have

$$c_n = \frac{J_n(kr_2) + T_n H_n^{(1)}(kr_2)}{J_\nu(k_1 r_2) + p_n N_\nu(k_1 r_2)} a_n \tag{62}$$

Thus, for this case of rotating fluid scatterer, the T matrix coefficients, are

$$T_{mn} = \delta_{mn} T_n \tag{63}$$

$$t_{mn} = \delta_{mn} t_n \tag{64}$$

where

$$t_n = \frac{k_1 q_n N_n(kr_2) - kN_n'(kr_2)}{k_1 q_n J_n(kr_2) - kJ_n'(kr_2)} \tag{65}$$

7. NORMALIZATION OF BAND FIELDS

As shown in the Appendix, the normalization is

$$\iint_{V_{0c}} dxdy\,|\psi|^2 + \iint_{V_{0r}} dxdy\,|\psi|^2 + \iint_{V_1} dxdy\,|\psi_1|^2 = 1 \tag{66}$$

The hexagonal cell is divided into three domains for volumetric integrations V_1, V_{0c}, and V_{0r} (Figure 3(a)).

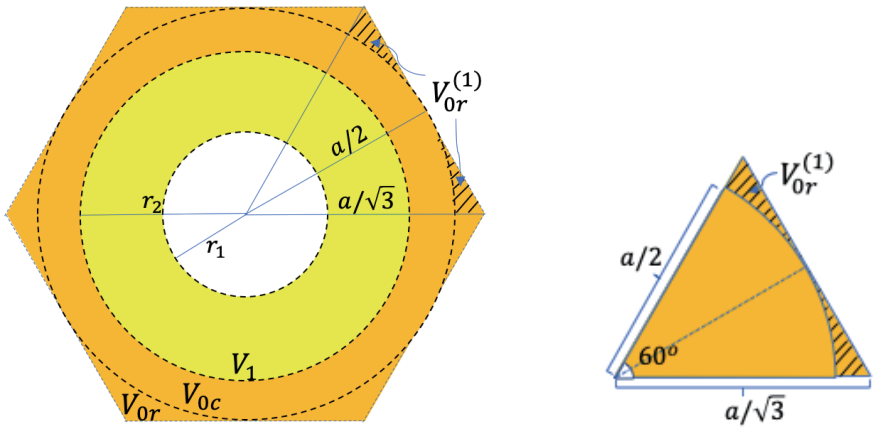

Figure 3. (a) V_1: $r_1 \leq r \leq r_2$; V_{0c}: $r_2 \leq r \leq a/2$; V_{0r}: remainder of hexagonal cell; $V_{0r}^{(1)}$: first section of V_{0r}. (b) $V_{0r}^{(1)}$: equilateral triangle with one-sixth of circle of radius $a/2$ subtracted from it.

The integrals are performed analytically using the indefinite integrals of Bessel function. For Z_p and B_p that are Bessel functions, Neumann functions and Hankel functions of first and second kind, the indefinite integrals are

$$I_1(p,\alpha,c,d,Z) = \int_c^d xZ_p(\alpha x)\,Z_p(\alpha x)\,dx = \frac{x^2}{2}\left[Z_p(\alpha x)\,Z_p(\alpha x) - Z_{p-1}(\alpha x)\,Z_{p+1}(\alpha x)\right] \tag{67}$$

$$\begin{aligned} I_2(p,\alpha,c,d,Z,B) &= \int_c^d xZ_p(\alpha x)\,B_p(\alpha x)\,dx \\ &= \frac{x}{2\alpha}\left[\alpha x Z_p(\alpha x)\,B_p(\alpha x) - \alpha x Z_{p-1}(\alpha x)\,B_{p+1}(\alpha x)\right. \\ &\quad \left. + p\left(Z_{p-1}(\alpha x)\,B_p(\alpha x) - Z_p(\alpha x)\,B_{p-1}(\alpha x)\right)\right]_{x=c}^{x=d} \end{aligned} \tag{68}$$

In V_0

$$\psi(\bar{r}) = \sum_{n=-N_{cyl}}^{N_{cyl}} \left[a_n^s H_n^{(1)}(kr) + a_n^c J_n(kr)\right] e^{in\theta} \tag{69}$$

We have set

$$a_n^s = 0 \text{ for } |n| > N_L \tag{70}$$

For V_{0c}, which is an angular region with inner radius r_2 and outer radius $\frac{a}{2}$

$$\begin{aligned} \iint_{V_{0c}} dxdy\,|\psi|^2 &= 2\pi\left\{\sum_{n=-N_{cyl}}^{N_{cyl}} \left[|a_n^s|^2\left(I_1\left(n,k,r_2,\frac{a}{2},J\right) + I_1\left(n,k,r_2,\frac{a}{2},N\right)\right)\right]\right. \\ &\quad \left. + 2\mathrm{Re}\left(a_n^s (a_n^C)^* I_2\left(n,k,r_2,\frac{a}{2},J,H^{(1)}\right)\right) + \sum_{n=-N_{cyl}}^{N_{cyl}} \left[|a_n^C|^2 I_1\left(n,k,r_2,\frac{a}{2},J\right)\right]\right\} \end{aligned} \tag{71}$$

The remainder region V_{0r} can be divided into 6 parts $V_{0r} = V_{0r}^{(1)} + V_{0r}^{(2)} + \ldots + V_{0r}^{(6)}$.

For each part it is the remainder of an equilateral triangle with the circular sector of radius $\frac{a}{2}$ subtracted from it (Figure 3(b)). The equilateral triangle has height $a/2$ and side $a/\sqrt{3}$.

For every circle of radius r, where $a/2 \le r \le a/\sqrt{3}$, the circle will intersect each of the six sides of the hexagon at two points.

For the north-east side of the hexagon, the two points are at $\theta = \gamma_H^N(r)$ and $\theta = \pi/3 - \gamma_H^N(r)$, where

$$\gamma_H^N(r) = \cos^{-1}\left(\frac{\sqrt{3} + 2\sqrt{\left(\frac{r}{a}\right)^2 - \frac{1}{4}}}{4\left(\frac{r}{a}\right)}\right) \tag{72}$$

Then referring to that as $V_{0r}^{(1)}$, we have

$$\begin{aligned}\iint_{V_{0r}^{(1)}} dxdy\,|\psi|^2 \;=\; & \int_{\frac{a}{2}}^{\frac{a}{\sqrt{3}}} drr \sum_{n=-N_{cyl}}^{N_{cyl}} \left(a_n^s H_n^{(1)}(kr) + a_n^c J_n(kr)\right) \\ & \sum_{m=-N_{cyl}}^{N_{cyl}} \left[\left(a_m^{s*} H_m^{(2)}(kr) + a_m^{c*} J_m(kr)\right) I_H^{(1)}(n-m,r)\right]\end{aligned} \tag{73}$$

where

$$I_H^{(1)}(n,r) = \left[\int_0^{\gamma_H^N(r)} d\theta + \int_{\pi/3-\gamma_H^N(r)}^{\pi/3} d\theta\right] e^{in\theta} \tag{74}$$

Adding the six parts and with rearrangement of limits of integrations, we have

$$\begin{aligned}\iint_{V_{0r}} dxdy\,|\psi|^2 \;=\; & \int_{\frac{a}{2}}^{\frac{a}{\sqrt{3}}} drr \sum_{n=-N_{cyl}}^{N_{cyl}} \left(a_n^s H_n^{(1)}(kr) + a_n^c J_n(kr)\right) \\ & \sum_{m=-N_{cyl}}^{N_{cyl}} \left[\left(a_m^{s*} H_m^{(2)}(kr) + a_m^{c*} J_m(kr)\right) I_H(n-m,r)\right]\end{aligned} \tag{75}$$

where

$$\begin{aligned}I_H(n,r) \;=\; & \left[\int_{\pi/3-\gamma_H^N(r)}^{\pi/3+\gamma_H^N(r)} d\theta + \int_{2\pi/3-\gamma_H^N(r)}^{2\pi/3+\gamma_H^N(r)} d\theta + \int_{\pi-\gamma_H^N(r)}^{\pi+\gamma_H^N(r)} d\theta + \int_{4\pi/3-\gamma_H^N(r)}^{4\pi/3+\gamma_H^N(r)} d\theta\right. \\ & \left. + \int_{5\pi/3-\gamma_H^N(r)}^{5\pi/3+\gamma_H^N(r)} d\theta + \int_{2\pi-\gamma_H^N(r)}^{2\pi+\gamma_H^N(r)} d\theta\right] e^{in\theta}\end{aligned} \tag{76}$$

Integrating, we have

$$I_H(n,r) = \begin{cases} \sum_{l=1}^{6} \left[\frac{e^{in\theta}}{in}\right]_{\theta=\frac{l\pi}{3}-\gamma_H^N(r)}^{\theta=\frac{l\pi}{3}+\gamma_H^N(r)} & \text{for } n \ne 0 \\ 12\gamma_H^N(r) & \text{for } n = 0 \end{cases} \tag{77}$$

and $\sum_{l=1}^{6}$ represents the summation over the six parts.

The formulas of integrations above of V_{0c} and V_{0r} are applicable to scatterer of arbitrary shape. For the case of the rotating fluid scatterer in the angular region of $r_1 \le r \le r_2$ which is V_1, the volumetric integral is

$$\begin{aligned}\iint_{V_1} dxdy\,|\psi_1|^2 \;=\; & 2\pi \sum_{n=-N_L}^{N_L} \left(|c_n|^2 I_1(\nu,k_1,r_1,r_2,J) + |d_n|^2 I_1(\nu,k_1,r_1,r_2,N)\right. \\ & \left. +2\mathrm{Re}\left(c_n^* d_n\right) I_2(\nu,k_1,r_1,r_2,J,N)\right)\end{aligned} \tag{78}$$

8. NUMERICAL RESULTS AND DISCUSSIONS

As in [2], we choose $r_1 = 0.2a$ and $r_2 = 0.4a$ where a is the lattice constant. We consider the K point in the Brillouin zone. Let the rotating angular velocity [2] be $\Omega = 0.2332 \times (2\pi c/a)$. We consider the hexagonal lattice with primitive lattice vectors $\bar{a}_1 = \frac{a}{2}\left(\sqrt{3}\hat{x} + \hat{y}\right)$ and $\bar{a}_2 = \frac{a}{2}\left(-\sqrt{3}\hat{x} + \hat{y}\right)$. In the hexagon of Figure 1, the vector from the southwest corner to the northeast corner is $\bar{a}_1$ while the vector from southeast corner to the northwest corner is $\bar{a}_2$. The reciprocal lattice vectors are $\bar{b}_1 = \frac{2\pi}{a}\left(\frac{1}{\sqrt{3}}\hat{x} + \hat{y}\right)$ and $\bar{b}_2 = \frac{2\pi}{a}\left(-\frac{1}{\sqrt{3}}\hat{x} + \hat{y}\right)$. We shall illustrate the calculations of the band eigenvalue and band field at the point K in the first Brillouin zone. At the point K, the Bloch vector is $\bar{k}_i = \frac{1}{3}\bar{b}_1 + \frac{1}{3}\bar{b}_2$. In the calculations, we let the lattice constant be $a = 1$ and speed of light $c = 1$. In the calculations of the broadband cylindrical wave coefficients $D_l(k)$, with imaginary extractions [40], the numerical parameters N_{spa}, N_{spe},ξ, and R are used in the evaluation of the broadband D_n coefficients. They are described in [40]. N_{spa} is the truncation number of the summation for the spatial part, and N_{spe} is for the spectral part. ξ is the imaginary wavenumber, and R is the radius of the circle used in the integration to get the D_n coefficients. N_{spa}, N_{spe}, ξ, and R are robust parameters that can have many choices. We have not optimized them. In this paper, we used N_{spa}= 4, N_{spe}= 4, ξ= 3, $R = 0.96$.

8.1. Eigenvalue and Normalized Eigenvector

The eigenvalue part is the CPU intensive part of the method. Thus, based on discussion in the previous section, we choose a low $N_L = 2$. Then $N_{DL} = 4$. We use the BBGF method to calculate $D_l(k)$, $l = 0, \pm 1, \pm 2, \ldots\ldots, \pm 4$. The first step is the set-up for the frequency independent part of $D_l(k)$ [40]. In the frequency scanning method, $D_l(k)$ are calculated in a broadband manner for many ks. In the bisection method, we only calculate $D_l(k)$ for the ks needed. We solve the eigenvalue problem from Equation (38), $\overline{\overline{\Lambda}}(k)\bar{a}^s = 0$.

The dimension of the matrix of the eigenvalue equation is $2N_L + 1 = 5$. The approach with bisection method in searching for k is the more efficient method. Table 1 shows CPU time for frequency scanning method and bisection method. Using the frequency scanning method, the absolute value of the determinant is shown in Figure 4. The figure clearly shows that the two eigenvalues are $f_N = 0.5527$ and $f_N = 0.5980$. This corresponds to the splitting of the degenerate eigenvalue for the rotating fluid [2, 39].

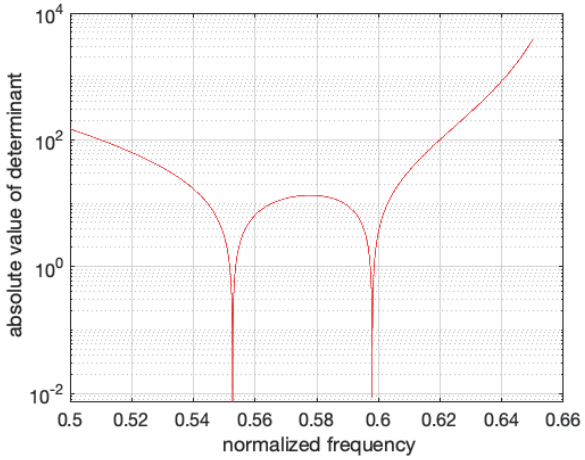

Figure 4. Frequency response of determinant of $\overline{\overline{\Lambda}}(k)$, showing 2 eigenvalues at 0.5527 and 0.5980.

The iterative approach with bisection method is applied in searching for k. The CPU time table is shown in Table 1.

The CPU table shows that using the bisection method, the CPU time including setup is merely 5 milliseconds for an eigenvalue. Simulation with COMSOLTM takes 2 seconds to compute the bands

Table 1. BBGF-KKR-MST method CPU time comparisons for computing band eigenvalue frequencies. $N_{spa} = 4$, $N_{spe} = 4$.

(CPU: 3.2 GHz 6-core Intel Core i7, Memory 32 GB 2667 MHz DDR4)

Method	*Set-up (milliseconds)*	*Number of bands*	N_L	*Number of frequencies*	D_l *and* $det(P)$ *(milliseconds)*	*Total CPU time (milliseconds)*
Frequency scanning	1.7	1	2	1000	124.9	126.6
Frequency scanning	2.6	1	3	1000	183.4	186
Bisection	2.1	1	2	14	2.9	5
Bisection	3.4	1	3	14	5.1	8.5

at a given point in the Brillouin zone. On the other hand, the BBGF-KKR-MST requires only 5 milliseconds for a single eigenvalue for the K point in this paper. We also show the band fields as computed by COMSOL. In the paper on topological photonics [41], we have used COMSOL and noted that the BBGF-KKR-MST method is significantly faster than COMSOL. In this paper, BBGF-KKR-MST method also shows much faster computation than COMSOL's, more than 100 times from Table 1. We next calculate the band field solution. For the eigenvalue $f_N = 0.5980$, we have $k = 3.757$. The eigenvector for the 5 by 5 eigenvalue problem is for the scattered field coefficients, $a_n^s = -2, -1, 0, 1, 2$. Only 2 coefficients are not small while other coefficients are small. The value is given in Table 2.

Table 2. Normalization of the eigenvector for the matrix equation.

Normalized eigenvector	$n = -2$	$n = 1$
a_n^s	0.2618	0.9651

The eigenvector is normalized so that $\sqrt{\left(a_{-2}^s\right)^2 + \left(a_1^s\right)^2} = 1$. Note that this normalization of the eigenvector for the matrix equation is not the normalization of the band field solution which will be calculated later.

8.2. Obtain Higher Order Cylindrical Waves

After the eigenvalue and eigenvector of the scattered field coefficients are obtained, we obtain higher order coefficients by the relation from Equation (44), $a_n^C = \sum_{m=-N_L}^{N_L} a_m^s \tilde{D}_{n-m}(k)$; $n = 0, \pm 1, \ldots, \pm N_L, \ldots, \pm N_{cyl}$.

The physical interpretation is that the exciting field ψ^{ex} is the scattered field from other cells into the $(0, 0)$ cell. This is made possible by the g_R part of the lattice Green's function giving the relation above. We choose $N_{cyl} = 5$. This means $N_L + N_{cyl} = 7$, then we need more $D_l(k = 3.757)$, $l = 0, \pm 1, \ldots, \pm 7$ for that single $k = 3.757$. They are tabulated below in Table 3 for those D_l that are significant values.

Then we apply the relation in Eq. (44) to obtain the higher order coefficients, $a_n^C n = 0, \pm 1, \ldots, \pm N_L, \ldots, \pm N_{cyl}$. For the scatterer region, we obtain the coefficients by using $c_n = \frac{J_n(kr_2) + T_n H_n^{(1)}(kr_2)}{J_n(k_1 r_2) + p_n N_n(k_1 r_2)} a_n^C$ and $d_n = p_n c_n, n = 0, \pm 1, \ldots, \pm N_{cyl}$. We also get higher order coefficients for a_n^s by using T matrix coefficients $T_n(k = 3.757)$.

The coefficients are tabulated below for values that are not small. The values in parenthesis are the results after band field normalized to be discussed later.

Table 3. Additional D_l coefficients at the eigen-wavenumber ($k = 3.757$) to be used for higher order cylindrical waves.

	$D_l\,(k = 3.757)$
$l = -6$	2.688
$l = -3$	1.169
$l = 0$	0.9407
$l = 3$	1.169
$l = 6$	2.688

8.3. Normalization of Wave Functions

We calculate the integrals of unnormalized band-fields. The values are below.

The normalization factor for the wave functions is $[\iint_{V_1} dxdy\,|\psi_1|^2 + \iint_{V_{0c}} dxdy\,|\psi|^2 + \iint_{V_{0r}} dxdy\,|\psi|^2]^{\frac{1}{2}} = 2.9268$. This factor is used to normalize the coefficients. The normalized coefficients are in parenthesis in Table 4. Integrals for unnormalized band-fields to calculate the normalization of band-fields are tabulated in Table 5.

Table 4. Higher order cylindrical wave coefficients, values based on normalized eigenvector; values in parenthesis are based on normalized band field solutions.

	$n = -5$	$n = -2$	$n = 1$	$n = 4$
a_n^C	$-i11.60$ $(-i3.964)$	$-0.262 - i5.499$ $(-0.089 - i1.879)$	$-0.965 - i4.856$ $(-0.330 - i1.659)$	$-i7.329$ $(-i2.504)$
c_n	$85.488 + i44.031$ $(29.209 + i15.044)$	$-i6.725$ $(-i2.298)$	$-i4.938$ $(-i1.687)$	$-i2.948$ $(-i1.007)$
d_n	$8.726 \times 10^{-8} - i4.494 \times 10^{-8}$ $(2.982 \times 10^{-8} - i1.536 \times 10^{-8})$	$i0.1603$ $(i0.0548)$	$i1.338$ $(i0.457)$	$i1.22 \times 10^{-4}$ $(i4.191 \times 10^{-5})$
a_n^s	4.004×10^{-6} (1.368×10^{-6})	0.2618 (0.08945)	0.9652 (0.3298)	-4.963×10^{-5} (-1.696×10^{-5})

Table 5. Integrals for unnormalized band-fields to calculate the normalization of band-fields.

	Integrals of unnormalized band-fields
$\iint_{V_1} dxdy\,\lvert\psi_1\rvert^2$	3.9513
$\iint_{V_{0c}} dxdy\,\lvert\psi\rvert^2$	3.5455
$\iint_{V_{0r}} dxdy\,\lvert\psi\rvert^2$	1.0692
sum	$8.5660 = (2.9268)^2$

8.4. Plotting the Fields

After the higher order coefficients are obtained, we can calculate the normalized fields throughout the entire cell $(0, 0)$. The normalized band field solution coefficients are given in Table 4.

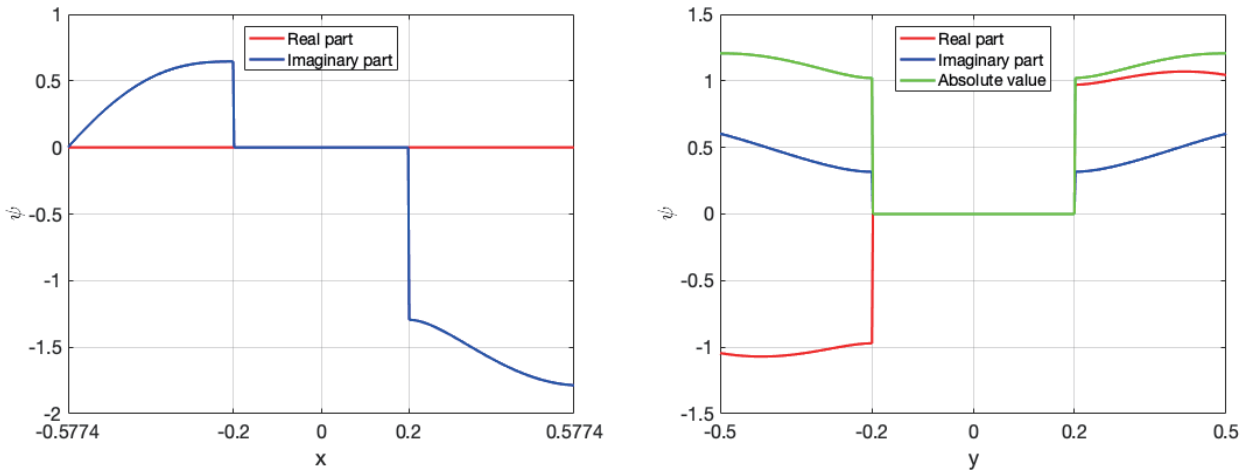

(a) (b)

Figure 5. Normalized field along (a) horizontal center line, (b) vertical center line of the $(0,0)$ cell.

In Figure 5(a), we plot the normalized fields for the horizontal center line, $y=0$ and $-a/\sqrt{3} \le y \le a/\sqrt{3}$. In Figure 5(b), we plot the normalized fields for the vertical centerline $x=0$ and $-a/2 \le y \le a/2$. We plot $|\psi_1|$ for $r_1 \le r \le r_2$ and $|\psi|$ for $r_2 \le r \le a/2$. For the region V_0

$$\psi(\bar{r}) = \sum_{n=-N_L}^{N_L} a_n^s H_n^{(1)}(kr)\, e^{in\theta} + \sum_{n=-N_{cyl}}^{N_{cyl}} a_n^C J_n(kr)\, e^{in\theta} \tag{79}$$

For the field inside the scatterer we use

$$\psi_1(\bar{r}) = \sum_{n=-N_L}^{N_L} \left[c_n J_\nu(k_1 r) + d_n N_\nu(k_1 r)\right] e^{in\theta} \tag{80}$$

For the vertical center line, the displacement between the North tip ($x=0$ and $y=a/2$) and the South tip ($x=0$ and $y=-a/2$) is $\bar{R} = a\hat{y} = \bar{a}_1 + \bar{a}_2$. The Bloch condition phase shift between the two tips for the K point in the Brillouin zone is $e^{i\bar{k}_i \cdot \bar{R}} = e^{i(\frac{1}{3}\bar{b}_1 + \frac{1}{3}\bar{b}_2)\cdot(\bar{a}_1+\bar{a}_2)} = e^{i\frac{4\pi}{3}}$. The results from Figure 5(b) are the band field $\psi = -1.0441 + i0.6036$ at $(x=0,\, y=-a/2)$ and the band field $\psi = 1.0441 + i0.6036$ at $(x=0,\, y=a/2)$. The phase shift between the two complex band fields is $-\frac{2\pi}{3}$ showing that the Bloch condition is obeyed. In using MST with cylindrical waves, the Bloch condition is implicit through the lattice Green's function expressed in cylindrical waves. We next plot in Figure 6 the band field within the entire hexagon of the $(0,0)$ cell. The field solutions are in good agreement with the previous method of BBGF-MoM.

Convergences of Cylindrical waves: The field patterns in Figure 6 clearly show that of cylindrical waves. Figure 6(a) shows the normalized field pattern at $f_N = 0.5980$ from BBG-KKR-MST method presented in this paper. For the comparison, Figure 6(b) shows the unnormalized field pattern at $f_N = 0.5925$ from VIE-MoM method. In [39], the fields within rotating fluid are shown. Here the results are extended to cover the entire hexagon. Figure 6(c) shows unnormalized field pattern at $f_N = 0.594$ from COMSOL. For BBG-KKR-MST and VIE-MoM methods, the acoustics differential equation in the rotating fluid region, Equation (46), is used. For COMSOL, based on options of equations in the software, the Navier-Stokes equation was used. Thus, a low order of 11 cylindrical waves is sufficient to characterize the fields in the cell $(0,0)$ of the hexagon. The fields in other cells can be obtained by applying the Bloch condition. In MST theory, the solutions of the eigenvalue problem have attained the accuracy if the scattered waves are calculated accurately. The coefficients of the scattered wave are the product of the exciting field coefficient with the T matrix coefficients. The

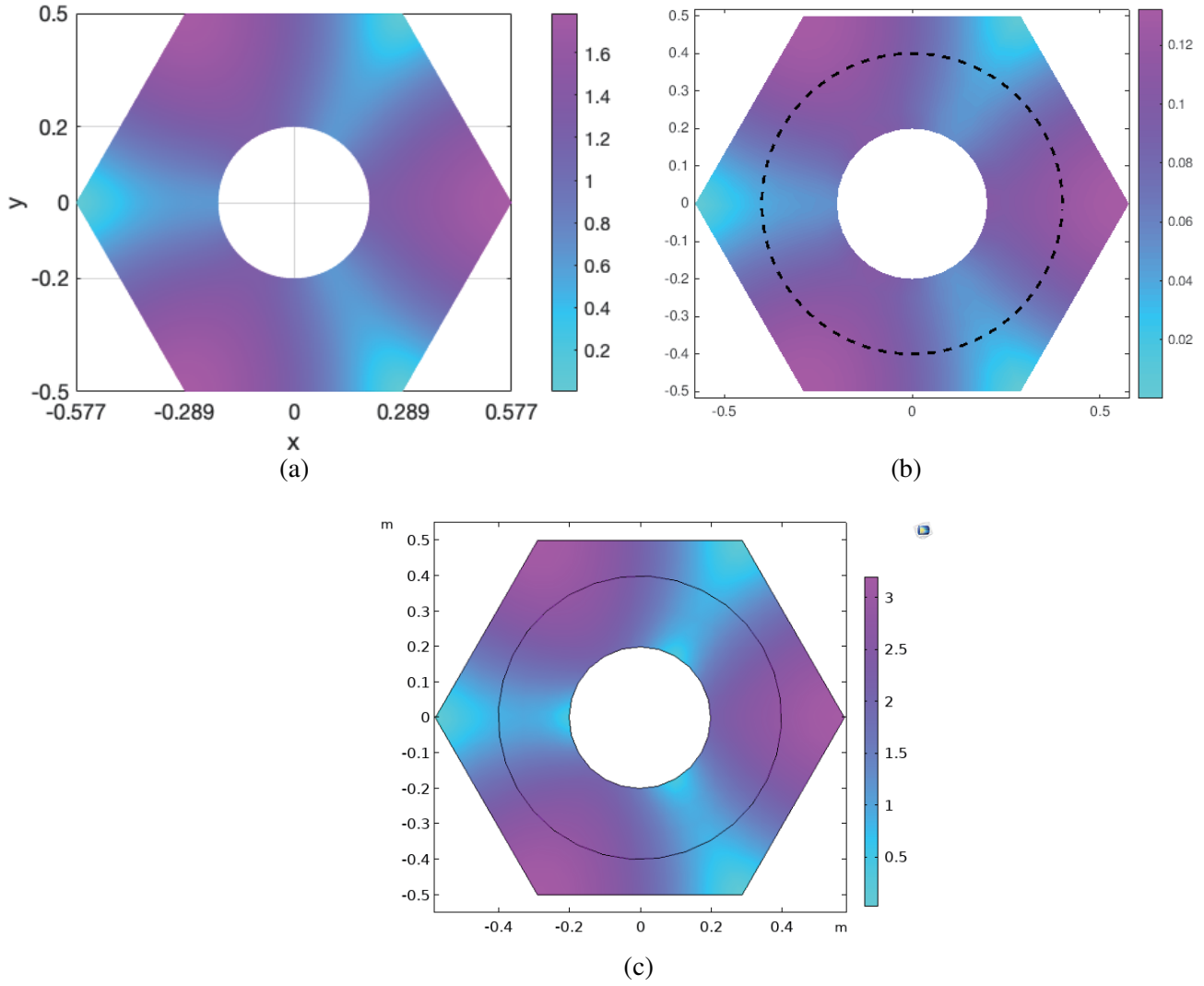

Figure 6. Field solution of the hexagon in cell $(0, 0)$ (a) normalized field at eigenvalue $f_N = 0.5980$ from BBG-KKR-MST method, (b) unnormalized field at eigenvalue $f_N = 0.5925$ from VIE-MoM method, (c) unnormalized field at eigenvalue $f_N = 0.594$ from COMSOL.

convergence of the scattered wave convergence depends on the convergence of the single scatterer T matrix with the cylindrical wave order n. The rule of thumb of n maximum is $1.5k$ to $2k$ times the radius. For the present problem a= 1 and radius of the scatterer is $r_2 = 0.4a$. We determined the band eigenvalue with $f_N = 0.5980$ and k= 3.757, then $1.5kr_2$= 2.25. Thus, the choice of n maximum which is N_L= 2 is sufficient for the convergence of the scattered wave. The cylindrical waves expansion has high computational efficiency because both the size of the scatterer and the size of the cell are smaller than or comparable to wavelength. The physical reason is that the field distribution in the cell is well represented by cylindrical waves. In previous papers [40, 41], we have compared the CPU time with COMSOL. The method of BBGF-KKR-MST is significantly faster than that of COMSOL.

The fields in Figure 6 are for $(0, 0)$ cell. For band-fields in other cells, they can be calculated by applying Bloch condition.

9. CONCLUSIONS

In this paper, we apply the BBGF-KKR-MST method to calculate band eigenvalue frequencies, band fields and the normalizations of band fields for topological acoustics. The advantages of the approach are (a) the low dimension of the eigenvalue matrix equation which is 5 by 5 for the first 2 bands in question, (b) the band field solutions are represented by 11 cylindrical wave coefficients, and (c) normalization of band field solutions are carried out without volumetric integrations. Accuracy of the solutions is demonstrated. In MST, the T matrix used is that of a single scatterer which is independent of the lattice and independent of the Bloch vector. Thus, for a general scatterer, the T matrix can be calculated separately in the frequency range of interest and then used for all lattices and Bloch vectors. This will further increase the computational efficiency of the BBGF-KKR-MST method. The BBGF-KKR-MST is a computational efficient method because (i) band fields are the results of multiple scattering; (ii) the field patterns are well characterized by cylindrical waves; and (iii) the BBGF facilitates the broadband search of the eigenvalue frequencies. With the band field solutions determined, we will calculate the BBGF with the plurality of scatterers [50–53].

APPENDIX A.

In this Appendix we derive the orthogonal relation and the normalization condition. For two bands β_1 and β_2 of the same $\bar{k}_i$, the two eigenvalues are $k_{\beta_1} = \omega^{(\beta_1)}/c$ and $k_{\beta_2} = \omega^{(\beta_2)}/c$. The wave functions $\psi_1^{(\beta_1)}$ and $\psi^{(\beta_1)}$ are for band β_1. The wave functions $\psi_1^{(\beta_2)}$ and $\psi^{(\beta_2)}$ are for band β_2.

$$\left(\nabla^2 + k_{\beta_1}^2\right)\psi_1^{(\beta_1)} = -i2\frac{\omega^{(\beta_1)}}{c^2}v_\theta(r)\frac{1}{r}\frac{\partial\psi_1^{(\beta_1)}}{\partial\theta} \tag{A1}$$

$$\left(\nabla^2 + k_{\beta_2}^2\right)\psi_1^{(\beta_2)} = -i2\frac{\omega^{(\beta_2)}}{c^2}v_\theta(r)\frac{1}{r}\frac{\partial\psi_1^{(\beta_2)}}{\partial\theta} \tag{A2}$$

Then

$$\begin{aligned}&\iint_{V_1} dxdy\left[\psi_1^{(\beta_2)*}\nabla^2\psi_1^{(\beta_1)} - \psi_1^{(\beta_1)}\nabla^2\psi_1^{(\beta_2)*}\right] + \left(k_{\beta_1}^2 - k_{\beta_2}^2\right)\iint_{V_1} dxdy\psi_1^{(\beta_2)*}\psi_1^{(\beta_1)}\\ &= \iint_{V_1} dxdy\left[-\psi_1^{(\beta_2)*}i2\frac{\omega^{(\beta_1)}}{c^2}v_\theta(r)\frac{1}{r}\frac{\partial\psi_1^{(\beta_1)}}{\partial\theta} - \psi_1^{(\beta_1)}i2\frac{\omega^{(\beta_2)}}{c^2}v_\theta(r)\frac{1}{r}\frac{\partial\psi_1^{(\beta_2)*}}{\partial\theta}\right]\end{aligned} \tag{A3}$$

Let $S = scatterer\ boundary$. Then

$$\begin{aligned}&\int_S dl\left[\psi_1^{(\beta_2)*}\frac{\partial\psi_1^{(\beta_1)}}{\partial n} - \psi_1^{(\beta_1)}\frac{\partial\psi_1^{(\beta_2)*}}{\partial n}\right] + \left(k_{\beta_1}^2 - k_{\beta_2}^2\right)\iint_{V_1} dxdy\psi_1^{(\beta_2)*}\psi_1^{(\beta_1)}\\ &= \iint_{V_1} dxdy\left[-\psi_1^{(\beta_2)*}i2\frac{\omega^{(\beta_1)}}{c^2}v_\theta(r)\frac{1}{r}\frac{\partial\psi_1^{(\beta_1)}}{\partial\theta} - \psi_1^{(\beta_1)}i2\frac{\omega^{(\beta_2)}}{c^2}v_\theta(r)\frac{1}{r}\frac{\partial\psi_1^{(\beta_2)*}}{\partial\theta}\right]\end{aligned} \tag{A4}$$

In region V_0

$$\left(\nabla^2 + k_{\beta_1}^2\right)\psi^{(\beta_1)} = 0 \tag{A5}$$

then

$$\left(\nabla^2 + k_{\beta_2}^2\right)\psi^{(\beta_2)} = 0 \tag{A6}$$

$$\iint_{V_0} dxdy\left[\psi^{(\beta_2)*}\nabla^2\psi^{(\beta_1)} - \psi^{(\beta_1)}\nabla^2\psi^{(\beta_2)*}\right] + \left(k_{\beta_1}^2 - k_{\beta_2}^2\right)\iint_{V_0} dxdy\psi^{(\beta_2)*}\psi^{(\beta_1)} = 0 \tag{A7}$$

Let $S_C = cell\ boundary$. Then

$$\begin{aligned}&\int_{S_C} dl\left[\psi^{(\beta_2)*}\frac{\partial\psi^{(\beta_1)}}{\partial n} - \psi^{(\beta_1)}\frac{\partial\psi^{(\beta_2)*}}{\partial n}\right]\\ &-\int_S dl\left[\psi^{(\beta_2)*}\frac{\partial\psi^{(\beta_1)}}{\partial n} - \psi^{(\beta_1)}\frac{\partial\psi^{(\beta_2)*}}{\partial n}\right] + \left(k_{\beta_1}^2 - k_{\beta_2}^2\right)\iint_{V_0} dxdy\psi^{(\beta_2)*}\psi^{(\beta_1)} = 0\end{aligned} \tag{A8}$$

The $\psi^{(\beta_1)}$ and $\psi^{(\beta_2)}$ have the same Bloch vector $\bar{k}_i$. Because of Bloch condition, and since we have the product of conjugate and the other function, the integration on the opposite sides of the cell boundary will cancel

$$\int_{S_C} dl \left[\psi^{(\beta_2)*} \frac{\partial \psi^{(\beta_1)}}{\partial n} - \psi^{(\beta_1)} \frac{\partial \psi^{(\beta_2)*}}{\partial n} \right] = 0 \tag{A9}$$

Then

$$-\int_S dl \left[\psi^{(\beta_2)*} \frac{\partial \psi^{(\beta_1)}}{\partial n} - \psi^{(\beta_1)} \frac{\partial \psi^{(\beta_2)*}}{\partial n} \right] + \left(k_{\beta_1}^2 - k_{\beta_2}^2 \right) \iint_{V_0} dxdy \psi^{(\beta_2)*} \psi^{(\beta_1)} = 0 \tag{A10}$$

On boundary S, the boundary conditions give

$$\int_S dl \left[\psi_1^{(\beta_2)*} \frac{\partial \psi_1^{(\beta_1)}}{\partial n} - \psi_1^{(\beta_1)} \frac{\partial \psi_1^{(\beta_2)*}}{\partial n} \right] = \int_S dl \left[\psi^{(\beta_2)*} \frac{\partial \psi^{(\beta_1)}}{\partial n} - \psi^{(\beta_1)} \frac{\partial \psi^{(\beta_2)*}}{\partial n} \right] \tag{A11}$$

The two corresponding terms in Eqs. (A4) and (A10) will cancel when the two equations are added. Thus, we have orthogonal relation for $\beta_1 \neq \beta_2$.

$$\begin{aligned} &\left(k_{\beta_1}^2 - k_{\beta_2}^2 \right) \left[\iint_{V_0} dxdy \psi^{(\beta_2)*} \psi^{(\beta_1)} + \iint_{V_1} dxdy \psi_1^{(\beta_2)*} \psi_1^{(\beta_1)} \right] \\ &+ \iint_{V_1} dxdy \left[\psi_1^{(\beta_2)*} i2 \frac{\omega^{(\beta_1)}}{c^2} v_\theta(r) \frac{1}{r} \frac{\partial \psi_1^{(\beta_1)}}{\partial \theta} + \psi_1^{(\beta_1)} i2 \frac{\omega^{(\beta_2)}}{c^2} v_\theta(r) \frac{1}{r} \frac{\partial \psi_1^{(\beta_2)*}}{\partial \theta} \right] = 0 \end{aligned} \tag{A12}$$

For $\beta_1 = \beta_2$

$$\begin{aligned} &\iint_{V_1} dxdy \left[\psi_1^{(\beta_1)*} i2 \frac{\omega^{(\beta_1)}}{c^2} v_\theta(r) \frac{1}{r} \frac{\partial \psi_1^{(\beta_1)}}{\partial \theta} + \psi_1^{(\beta_1)} i2 \frac{\omega^{(\beta_1)}}{c^2} v_\theta(r) \frac{1}{r} \frac{\partial \psi_1^{(\beta_1)*}}{\partial \theta} \right] \\ &= i2 \frac{\omega^{(\beta_1)}}{c^2} \int_{r_1}^{r_2} dr r v_\theta(r) \frac{1}{r} \int_0^{2\pi} d\theta \frac{\partial \psi_1^{(\beta_1)} \psi_1^{(\beta_1)*}}{\partial \theta} = 0 \end{aligned} \tag{A13}$$

Thus, we set

$$\iint_{V_0} dxdy \psi^{(\beta_1)*} \psi^{(\beta_1)} + \iint_{V_1} dxdy \psi_1^{(\beta_1)*} \psi_1^{(\beta_1)} = 1 \tag{A14}$$

as the normalization condition.

ACKNOWLEDGMENT

We thank Zhaoyang Feng for making the calculations of COMSOL in this paper.

REFERENCES

1. Wang, Z., Y. D. Chong, J. D. Joannopoulos, and M. Soljacic, "Reflection-free one-way edge modes in a gyromagnetic photonic crystal," *Phys. Rev. Lett.*, Vol. 100, 013905, 2008.
2. Yang, Z., F. Gao, X. Shi, X. Lin, Z. Gao, Y. Chong, and B. Zhang, "Topological acoustics," *Phys. Rev. Lett.*, Vol. 114, 114301, 2015.
3. Xue, H., Y. Yang, G. Liu, F. Gao, Y. Chong, and B. Zhang, "Realization of an acoustic third-order topological insulator," *Phys. Rev. Lett.*, Vol. 122, 244301, June 2019.
4. Ao, X., Z. Lin, and C. T. Chan, "One way edge modes in a magneto-optical honeycomb photonic crystal," *Phys. Rev. B*, Vol. 80, 033105, 2009.
5. Feng, Z., S. Tan, L. Tsang, and E. Li, "Band characterization of topological photonic crystals using the broadband Green's function technique," *Optics Express*, Vol. 28, No. 19, 27223, 2020.

6. Ho, K. M., C. T. Chan, and C. M. Soukoulis, "Existence of a photonic gap in periodic dielectric structures," *Phys. Rev. Lett.*, Vol. 65, 3152–3155, 1990.
7. Leung, K. M. and Y. F. Liu, "Full vector wave calculation of photonic band structures in face-centered-cubic dielectric media," *Phys. Rev. Lett.*, Vol. 65, 2646–2649, 1990.
8. Plihal, M. and A. A. Maradudin, "Photonic band structure of two-dimensional systems: The triangular lattice," *Phys. Rev. B*, Vol. 44, 8565–8571, 1991.
9. Joannopoulos, J. D., S. G. Johnson, J. N. Winn, and R. D. Meade, *Photonic Crystals: Molding the Flow of Light*, Princeton University Press, 2011.
10. Fan, S., P. R. Villeneuve, and J. D. Joannopoulos, "Large omnidirectional band gaps in metallodielectric photonic crystals," *Phys. Rev. B*, Vol. 54, 11245–11251, 1996.
11. Zhao, R., G. D. Xie, M. L. N. Chen, Z. Lan, Z. Huang, and W. E. I. Sha, "First-Princip calculation of Chern number in gyrotropic photonic crystals," *Optics Express*, Vol. 28, 4638, 2020.
12. Nicolet, A., S. Guenneau, C. Geuzainec, and F. Zollaa, "Modelling of electromagnetic waves in periodic media with finite elements," *Journal of Comp. and Appl. Math.*, Vol. 168, 321–329, 2004.
13. Jin, J. M., *Finite Element Method in Electromagnetics*, 3rd Edition, Wiley, 2014.
14. Korringa, J., "On the calculation of the energy of a Bloch wave in a metal," *Physica*, Vol. 13, 392–400, 1947.
15. Kohn, W. and N. Rostoker, "Solution of the Schrodinger Equation in periodic lattices with an application to metallic lithium," *Phys. Rev.*, Vol. 94, 1111–1120, 1954.
16. Leung, K. M. and Y. Qiu, "Multiple-scattering calculation of the two-dimensional photonic band structure," *Phys. Rev. B*, Vol. 48, 7767–7771, 1993.
17. Foldy, L. L., "The multiple scattering of waves. I. General theory of isotropic scattering by randomly distributed scatterers," *Phys. Rev.*, Vol. 67, 107–119, 1945.
18. Lax, M., "Multiple scattering of waves," *Rev. Mod. Phys.*, Vol. 23, 287–310, 1951.
19. Liu, Z., C. T. Chan, P. Sheng, A. L. Goertzen, and J. H. Page, "Elastic wave scattering by periodic structures of spherical objects: Theory and experiment," *Phys. Rev. B*, Vol. 62, 2446–2457, 2000.
20. Tsang, L., C. E. Mandy, and K. H. Ding, "Monte Carlo simulations of the extinction rate of dense media with randomly distributed dielectric spheres based on solution of Maxwell's equations," *Optics Letters*, Vol. 17, 314–316, 1992.
21. Tse, K. K., L. Tsang, C. H. Chan, K. H. Ding, and K. W. Leung, "Multiple Scattering of Waves by Dense Random Distribution of Sticky Particles for Applications in Microwave Scattering by Terrestrial Snow," *Radio Science*, Vol. 42, 2007.
22. Chen, H. F., Q. Li, L. Tsang, C. C. Huang, and V. Jandhyala, "Analysis of a large number of vias and differential signaling in multilayered structures," *IEEE Transactions on Microwave Theory and Techniques*, Vol. 51, 818–829, 2003.
23. Tsang, L., H. F. Chem, C. C. Huang, and V. Jandhyala, "Methods for modeling interactions between massively coupled multiple vias in multilayered electronic packaging structures," US patent, Number 7149666, 2006.
24. Mishchenko, M. I., L. D. Travis, and A. A. Laci's, *Multiple Scattering of Light by Particles, Radiative Transfer and Coherent Backscattering*, Cambridge University Press, 2006.
25. Mishchenko, M. I., L. Liu, D. W. Mackowski, B. Cairns, and G. Videen, "Multiple scattering by random particulate media: Exact 3D results," *Optics Express*, Vol. 15, 2822–2836, 2007.
26. Waterman, P. C. and R. Truell, "Journal of mathematical physics," *Journal of Mathematical Physics*, Vol. 2, 512–537, 1961.
27. Faulkner, J. S., G. Malcolm, and Y. Wang, *Multiple Scattering Theory, Electronic Structure of Solids*, IOP Press, 2018.
28. Lai, Y., Z. Q. Zhang, C.H. Chan, and L. Tsang, "Gap structures and wave functions of classical waves in large-sized two-dimensional quasiperiodic structures," *Phys. Rev. B*, Vol. 74, 054305, 2006.
29. Van Hove, M. A. and S. Y. Tong, "Surface crystallography by LEED: Theory, computation and structural results," *Springer Theory in Chemical Physics*, 1979.

30. Xu, M.-L., J. J. Barton, and M. A. Van Hove, "Electron scattering by atomic chains: Multiple-scattering effects," *Phys. Rev. B*, Vol. 39, 8275, 1989.
31. Gavaza, G. M., Z. X. Yu, L. Tsang, C. H. Chan, S. Y. Tong, and M. A. van Hove, "Efficient calculation of electron diffraction for the structural determination of nanomaterials," *Phys. Rev. Lett.*, Vol. 97, 055505/1–4, 2006.
32. Lubatsch, A. and R. Frank, "Self-consistent quantum field theory for the characterization of complex random media by short laser pulses," *Phys. Rev. Res.*, Vol. 2, 013324, 2020.
33. Chan, C. H. and L. Tsang, "A sparse-matrix canonical-grid method for scattering by many scatterers," *Microwave and Optical Technology Letters*, Vol. 8, 114–118, 1995.
34. Yang, Z., F. Gao, X. Shi, X. Lin, Z. Gao, Y. Chong, and B. Zhang, "Topological acoustics," *Phys. Rev. Lett.*, Vol. 114, 114301, 2015.
35. Xue, H., Y. Yang, G. Liu, F. Gao, Y Chong, and B. Zhang, "Realization of an acoustic third-order topological insulator," *Phys. Rev. Lett.*, Vol. 122, 244301, 2019.
36. Feng, Z. and S. Tan, "Modeling reáection-free one-way edge modes using foldy-lax multiple scattering theory," *2021 International Applied Computational Electromagnetics Society Symposium (ACES)*, August 2021.
37. Tsang, L., "Broadband calculations of band diagrams in periodic structures using the broadband Green's function with low wavenumber extraction (BBGFL)," *Progress In Electromagnetics Research*, Vol. 153, 57–68, 2015.
38. Tsang, L. and S. Tan, "Calculations of band diagrams and low frequency dispersion relations of 2D periodic dielectric scattering using broadband Green's function with low wavenumber extraction (BBGFL)," *Optics Express*, Vol. 24, 945–965, 2016.
39. Tan, S. and L. Tsang, "Band structures and modal fields in topological acoustics: An integral equation formulation," *IEEE Antennas and Propagation Symposium*, Atlanta, 2019.
40. Gao, R., L. Tsang. S. Tan, and T.-H. Liao, "Band calculations using broadband Green's functions and the KKR method with applications to magneto-optics and photonic crystals," *Journal of Optical Society of America B*, Vol. 37, 3896–3907, 2020.
41. Gao, R., L. Tsang, S. Tan, and T.-H. Liao, "Broadband Green's function-KKR-multiple scattering method for calculations of normalized band-field solutions in magnetic-optics crystals," *Journal of Optical Society of America B*, Vol. 38, 3159–3171, 2021.
42. Tan, S. and L. Tsang, "Efficient broadband evaluations of lattice green's functions via imaginary wavenumber components extractions," *Progress In Electromagnetics Research*, Vol. 164, 63–74, 2019.
43. Sanamzadeh, M. and L. Tsang "Fast and broad band calculation of the dyadic Green's function in the rectangular cavity; An imaginary wave number extraction technique," *Progress In Electromagnetic Research C*, Vol. 96, 243–258, 2019.
44. Tsang, L., J. A. Kong, K. H. Ding, and C. O. Ao, *Scattering of Electromagnetic Waves, Vol. 2: Numerical Simulations*, 705, Wiley Interscience, 2001.
45. Tsang, L. and J. A. Kong, *Scattering of Electromagnetic Waves, Vol. 3: Advanced Topics*, 413, Wiley Interscience, 2001.
46. Xu, X., D. Liang, L. Tsang, C. M. Andreadis, E. G. Josberger, D. P. Lettenmaier, D. W. Cline, and S. H. Yue, "Active remote sensing of snow using NMM3D/DMRT and comparison with CLPX II airborne data," *IEEE Journal of Selected Topics in Applied Earth Observations and Remote Sensing*, Vol. 3, No. 4, 689–697, December 2010.
47. Huang, H., L. Tsang, A. Colliander, R. Shah, X. Xu, and S. H. Yueh, "Multiple scattering of waves by complex objects using hybrid method of T-matrix and foldy-lax equations using vector spherical waves and vector spheroidal waves," *Progress In Electromagnetic Research*, Vol. 168, 87–111, 2020.
48. Gu, W., L. Tsang, A. Colliander, and S. H. Yueh, "Wave propagation in vegetation field using a hybrid method," *IEEE Transactions on Antennas and Propagation*, early access, 2021.
49. Gradshteyn, I. S. and I. M. Ryzhik, *Table of Integrals, Series, and Products*, Academic Press, 2007.

50. Tan, S. and L. Tsang, "Green functions, including scatterers, for photonic crystals and metamaterials," *Journal of Optical Society of America B*, Vol. 34, 1450–1458, 2017.
51. Tan, S. and L. Tsang, "Scattering of waves by a half-space of periodic scatterers using broadband Green's function," *Opt. Lett.*, Vol. 42, No. 22, 4667–4670, November 2017.
52. Tsang, L., K.-H. Ding, and S. Tan, "Broadband point source Green's function in a one-dimensional infinite periodic lossless medium based on BBGFL with modal method," *Progress In Electromagnetics Research*, Vol. 163, 51–77, 2018.
53. Tsang, L. and S. Tan, "Full wave simulations of photonic crystals and metamaterials using the broadband green's functions," US patent number 11,087,043, August 10, 2021.